Particle swarm optimization of nanoantenna-based infrared detectors

EDGAR BRIONES,[1,*] RIEMANN RUIZ-CRUZ,[1] JOEL BRIONES,[2] NATALIA GONZALEZ,[1] JORGE SIMON,[3] MAYELA ARREOLA,[1] AND GREGORIO ALVAREZ-ALVAREZ[1]

[1]*Department of Mathematics and Physics, The Jesuit University of Guadalajara, Jalisco 45604, Mexico*
[2]*Centro de Investigaciones en Optica, Leon, Guanajuato 37150, Mexico*
[3]*Centro de Investigación, Innovación y Desarrollo en Telecomunicaciones, Universidad Autónoma de Zacatecas, Zacatecas 98000, Mexico*
*edgarbriones@iteso.mx

Abstract: The multi-resonant response of three-steps tapered dipole nano-antennas, coupled to a resistive and fast micro-bolometer, is investigated for the efficient sensing in the infrared band. The proposed devices are designed to operate at 10.6 μm, regime where the complex refractive index of metals becomes important, in contrast to the visible counterpart, and where a full parametric analysis is performed. By using a particle swarm algorithm (PSO) the geometry was adjusted to match the impedance between the nanoantenna and the micro-bolometer, reducing the return losses by a factor of 650%. This technique is compared to standards matching techniques based on transmission lines, showing better accuracy. Tapered dipoles therefore open the route towards an efficient energy transfer between load elements and resonant nanoantennas.

1. Introduction

In the recent years, great efforts have been addressed in improving thermal imagining devices, due to their increasingly wider commercial, medical and military applications [1,2]. Nowadays, thermal cameras exist thanks to the use of uncooled thermo-resistive detectors so-called bolometers [3,4]. These detectors are the most sensitive devices able to image in the long-wavelenght infra-red (LWIR) regime (band) (7-14 μm). Several materials such as the vanadium oxide (VOx) or the amorphous silicon (α-Si) are used as the most common commercial bolometers due to their high temperature coefficient of resistance (TCR) and relatively low-cost [5–7]. Nevertheless, novel materials displaying enhanced properties are currently being investigated as new bolometers candidates [8–10].

The receiving properties of the uncooled bolometer can be increased by coupling it to the feed point of a receiving antenna [11–13]. In this type of coupled device, the antenna collects the incident radiation as an alternate current induced along its volume. The bolometer subsequently detects such a resonance mode due to the ohmic losses that increase its temperature. By using this type of architecture, bolometers can be taken to the micrometer scale, enhancing thus their speed and sensitivity [14,15].

Despite the attractive functionalities of antenna-coupled micro-bolometers, their sensitivity remains relatively poor in experimentally realized devices [16]. The main reasons are: (a) the steady dissipation of heat towards the surroundings, which decreases the temperature changes in the bolometers [17–20], and (b) the impedance mismatch between the bolometer and the antennas, which introduces energy transfer problems between both elements [16,21]. The micrometer-sized bolometers exhibit high resistance values; for instance, when thin films made of Nb (70nm) and VOx (60nm) are used as bolometric materials, the resistance can reach values around 3.0 kΩ and 1.2 kΩ respectively [16,21]. In this paper, we address efforts to reduce the losses of sensitivity due to the mismatch issue.

Recently, a novel type of antenna design, the so-called tapered dipoles [22,23], in which the width of the arms forming the dipole decreases stepwise, was introduced aiming to improve the impedance coupling of infrared antennas to high-resistive load elements. For instance, these structures were used to improve the energy transfer between the antenna and metal-insulator-metal rectifying diodes of 500 Ω impedance, operating in the visible regime (λ = 500nm) [22]. These types of antennas are devices that exhibit a multi-resonant behavior in their band of operation [24]. In this work, we exploit such a multi-resonant response, which can be tuned via their geometrical parameters, in order to meet specific impedance requirements at the antennas terminals. Their extended use to the LWIR regime (λ = 10.6 μm), where effects of refractive index become important (e.g. the refractive index of titanium increases from n^* = 2.6 + j 3.58 (λ = 600nm) to n^* = 4.1 + 20.3j (λ = 10.6 μm), and silver from n^* = 0.05 + 3.13j (λ = 500nm) to n^* = 7.87 + 77.28j (λ = 10.6 μm)) [25], is herein analyzed.

In this study, the authors make use of a tapered dipole as a means to better match the impedance of high-resistive micro-bolometers in the LWIR band. A three-step tapered dipole made of titanium (Ti), material chosen by its short skin depth [25], is used as the receiving antenna. The impedance and the performance of the device are evaluated by performing numerical simulations via the COMSOL Multi-Physics platform (ver. 5.3a), a software package based on the finite-element method. A powerful algorithmic tool, the so-called particle swarm optimization (PSO) algorithm [26–28], externally linked to the numerical solver, is employed to find the values of the parameters that match the best the impedance of the micro-bolometers. Micro-bolometers with a resistance of 500 Ω are considered here as a case of study.

The PSO is an algorithm that aims to optimize cost functions whose solution via analytical methods is very complex to find. The PSO algorithm thus proposes an initial set of possible solutions (known as *particle swarm*) for the optimization problem. This set is subsequently evolved based on social rules, where the particle swarm is moved around the best particle solution iteratively, the best result of a swarm particle being the solution of the algorithm. In this work, the cost function is related to the results of the simulation of a tapered nanoantenna. The PSO algorithm is implemented in MatLab and the tapered antenna simulation is implemented in COMSOL Multiphysics. Then, the Matlab routine executing the PSO algorithm generates the antenna parameter configurations as possible solutions to the cost function, which are sent to COMSOL for the antenna to be simulated. Once the simulation is completed, both the frequency response (S_{11} in decibels) and the antenna impedance (Z_{in}) are returned to MatLab so that the cost function is evaluated and the PSO algorithm decides the new swarm for the next iteration. The interaction between MatLab and COMSOL is easily done using the LiveLink MatLab tool provided by COMSOL.

2. Impedance and resonance modes of conventional half-wave dipoles

In order to perform this study, we first analyze the complex impedance $Z_{in} = R + X^*j$ of conventional half-wave dipoles, since the tapered dipole geometry is based on the geometry of conventional dipoles. A schema of the conventional dipole hereby considered is shown in Fig. 1(a). The dipole is lying on a substrate that consists of a silicon dioxide layer (SiO_2 1μm thick) on the top of a silicon wafer (Si semi-infinite), while the upper half-space is vacuum. The silicon dioxide layer is thick enough to electrically isolate and reduce the dielectric contribution of the underlying Si substrate. We consider the case of a Ti dipole with length L = 2.2 μm, width W = 200 nm, thickness T = 100 nm and a center gap G = 100 nm; these dimensions are appropriately tuned to recover the infrared wavelength around λ = 10.6 μm (28.3 THz). The resonance length of the dipole is then shorter than the free-space length (5.3 μm) due to the dielectric contribution of the SiO_2 layer. Since the manufacture of these devices requires the use of advanced electron beam lithography and thin-film metal

deposition techniques [29–31], the experimental realization of devices is out of the scope of the contribution.

In the LIWR regime, both the impedance and the resonant modes of the Ti dipoles substantially differ from their microwave counterpart, because of the strong dispersion in metals at optical frequencies [32,33]. This dispersion in turn reduces the effective resonance wavelengths from the conventional $\lambda/2$ resonance [33], and modifies the conventional 73-Ω impedance value. In order to evaluate the impedance in this regime, a numerical model that takes into account the experimental dielectric functions of the materials was built [25].

In order to perform the numerical simulations, the antennas are considered to be in the transmit mode, so they are excited at the gap by an alternate source [34]. A lumped port with a reference impedance $Z_{ref} = 500$ Ω is used for both purposes, to excite the antenna ($V_{AC} = 1$ V), and to introduce the impedance mismatch of high-resistive micro-bolometers. In the transmit mode, the antenna will radiate electromagnetic energy towards their surroundings (substrate and the vacuum), hence, in order to prevent reflections from the simulation environment (the boundaries) absorption layers have been employed. In the transmit mode, the impedance Z_{in} is easily evaluated by the ratio of the voltage V (across the gap G) to the complex current I obtained from the simulations, with $Z_{in} = V/I$. Both components of the impedance, real (R) and imaginary (X) parts, are plotted as a function of the excitation frequency in Fig. 1(b).
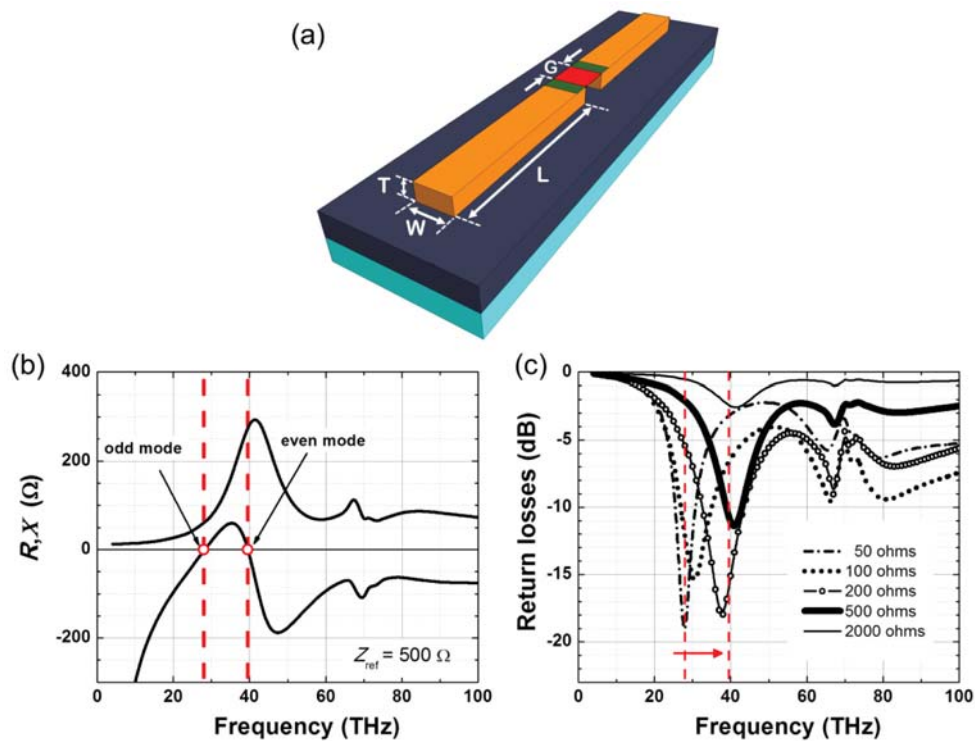

Fig. 1. Half-wave dipole nano-antenna coupled to a nano-bolometer. (a) Schematic representation of the nano-antenna, defining its geometrical parameters *width* W, *length* L and *thickness* T. The nano-bolometer is freestanding-bridge-like on the dipole elements; with the antenna lying on a Si//SiO$_2$ substrate. (b) Input impedance of the dipole-antenna as a function of the frequency; with R being the real and X the imaginary parts of the impedance. (c). Frequency dependence of the input return loss (S$_{11}$) for several port-resistance values.

Once the input impedance of the Ti dipoles was evaluated, the resonant modes of the antennas in the LWIR regime can be easily determined by identifying the zeros of the

reactance-frequency plot, open circles in Fig. 1(b). The numerical results show that the fundamental resonance (first zero of the reactance plot) appears at ~28 THz. For this resonance mode, the amplitude of the impedance is relatively low (~60 Ω). In general, half-wave dipoles exhibit low impedance at odd multiples of the fundamental mode. On the other hand, at even multiples of the fundamental resonance the amplitude of the impedance is relatively high, a few hundreds of ohms, for instance Z_{in}~280 Ω at 39 THz. To address the use of dipoles as infrared detectors it must be noted that, although both *odd* and *even* harmonics are resonant, feeding the dipoles on the *odd* resonances with resistive sensor-elements such as the micro-bolometers is not a good choice since the energy transfer will drop much more than in the even ones, as can be seen in Fig. 1(c). Having in mind this fact, we address efforts in this work with the aim of exploiting the natural resistance of the even resonances for the case where high resistive load elements are present.

3. Return losses and mismatch impedance of half-wave dipoles

Once the impedance of the Ti dipole was obtained, the inconveniences introduced by the 500-Ω port on the performance of the infrared detector are analyzed. In order to perform this task, we evaluate the return loss S_{11} in decibels [dB] as a function of the frequency of the port, parameter shown in the bold graph in Fig. 1(c). The measured parameter is the power loss in the returned/reflected signal between the dipole and the port, so that higher absolute values of the parameter mean a better match and energy transfer.

Results show that there are considerable losses of power (S_{11}~-2 decibels) by reflection at the odd resonance mode (28 THz), the mode where the antenna-based detector should exhibit its higher performance due to the length of the antenna. It must be noted that the losses by reflection are minimal (S_{11}~-11.5 decibels) for a frequency band around 42 THz, a little above the even resonance mode. This is due to the better match of the port on the even mode. At this regard, several types of (experimentally realized) LWIR detectors and harvesting devices, based on resistive metal-insulator-metal diodes, could also be used to sense in an efficient manner radiation of higher frequencies by using the even mode [35,36].

In order to get an insight on this fact, the return losses for several port resistances (50, 100, 200, 500, and 2000 Ω) were evaluated and compared in Fig. 1(c). On the one hand, the position of the minimal losses by reflection depends on the resistance of the port. In this regard, devices with port of higher impedance will operate at bands of higher frequency. On the other hand, devices with best performance are those that match the better the impedance of the odd and even resonances of the dipole, such as the case of the port of 50 ohms and 200 ohms.

It is worth to mention that the dimensions of the conventional Ti dipole can be tuned to shift the even mode (which exhibits a high-resistance) towards frequencies around 28.3 THz, and therefore use this mode to better match the impedance of the port. This strategy will thus lead to dipoles with larger physical lengths L. Nevertheless, increasing the size of the antenna components does not contribute to the high integration desired in microelectronics devices. In this regard, tapered dipoles also introduce a manner to change the effective resonance length of a dipole without changing the physical length, as we will discuss below.

4. Tapered dipoles and geometrical characteristics

To overcome the issue concerning the mismatch between the infrared antenna and the 500-Ω resistance port, tapered dipoles (shown in Fig. 2) are used as a strategy to tune the impedance of the antennas (without changing the physical length of the devices). The tapered nanoantenna design consists of a conventional Ti dipole with two additional steps of smaller size inserted in each of its arms. As mentioned above, these nanostructures support resonant modes of higher-order, which induce on the dipole a multi-resonant behavior. This multi-resonant behavior can be tuned by adjusting the geometrical parameters and is herein intentionally exploited to meet impedance requirements.
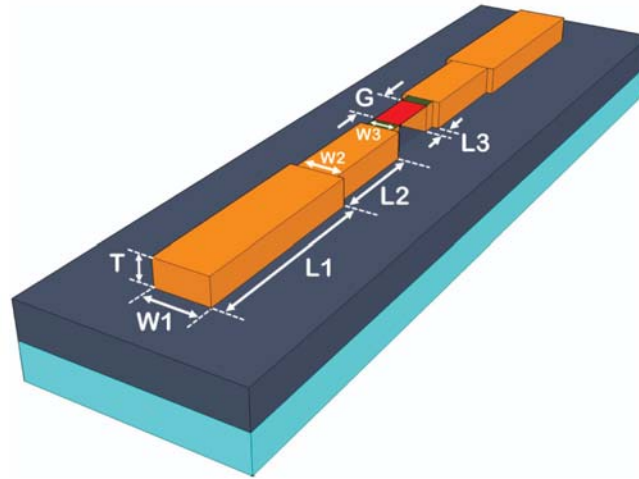
Fig. 2. Schematic representation of the three-steps tapered dipole antenna, defining its geometrical parameters *width* W, *length* L and *thickness* T, for each of the three steps. The nano-bolometer is freestanding-bridge-like on the dipole elements; with the antenna lying on a Si//SiO$_2$ substrate.

The geometrical description of the studied tapered dipole requires the use of an eight-dimensional space, defined by the length (L_1, L_2, L_3), the width (W_1, W_2, W_3) and the thickness T of the tapered sections, as well as the gap distance G of the dipole. Each of these parameters affects the value of the impedance; their relative importance being determined by the PSO algorithm will be described in the next section. Prior to it, we evaluate the performance of a few arbitrary geometries in order to get some insight on the parameters that affect the impedance the most. The dimensions of the considered geometries, defined as types A to E, are listed in Table 1. It must be noted the length of all the geometries does not change ($L = 2.2$ μm), and all of them keep fixed both the thickness $T = 100$ nm and the gap $G = 100$nm.

Table 1. Geometrical parameters for the three-steps tapered dipole antennas

Antenna parameters	Type A	Type B	Type C	Type D	Type E
W_1	300 nm	250 nm	200 nm	200 nm	220 nm
W_2	200 nm	140 nm	120 nm	70 nm	100 nm
W_3	150 nm	80 nm	40 nm	50 nm	80 nm
L_1	750 nm	600 nm	100 nm	100 nm	100 nm
L_2	200 nm	350 nm	500 nm	500 nm	500 nm
L_3	100 nm	100 nm	450 nm	450 nm	450 nm
T	100 nm	100 nm	100 nm	100 nm	100 nm
G	100 nm	100 nm	100 nm	100 nm	100 nm

5. Characteristic impedance trends

The impedance corresponding to the different geometries is presented in Fig. 3(a) and is compared with the impedance of a conventional dipole (dashed line). It is found that the steps introduced in the conventional dipole results in both, the shift of the resonant modes towards lower frequencies and an increase of the impedance. On the one hand, the physical origin of the shift can be understood by considering the effective path length of the resonant current. By introducing the steps, the effective length increases leading to longer effective wavelengths. On the other hand, by comparing the dimensions of the tapered geometries with the higher impedances, the geometries of the types C and D, it can be seen the amplitude

depends on the width of the two steps closest to the gap W_2, W_3, the narrower the steps the higher the impedance.

Due to their thin-film structure, not only the lateral geometry of the nanoantennas affects the resonant modes but the thickness too, which becomes a relevant factor. In order to highlight the latter we have obtained the impedance of a fixed geometry with different thickness, shown in Fig. 3(b). Particularly, we have varied the thickness of the geometry A (keeping fixed the other parameters). The results show that thinner antennas exhibit higher impedances and resonant modes shifted towards lower frequencies. For small thickness, the charge of the top surface and the charge on the bottom surface are highly correlated to each other. Strong coupling results in a larger effective total charge, which in turn increases the effective resonant wavelengths [37]. For larger thickness, the charge of the top and bottom surfaces decouples, acting more like separates dipoles that exhibit resonant modes at higher frequencies. Geometries of the types B to E exhibit a similar behavior.
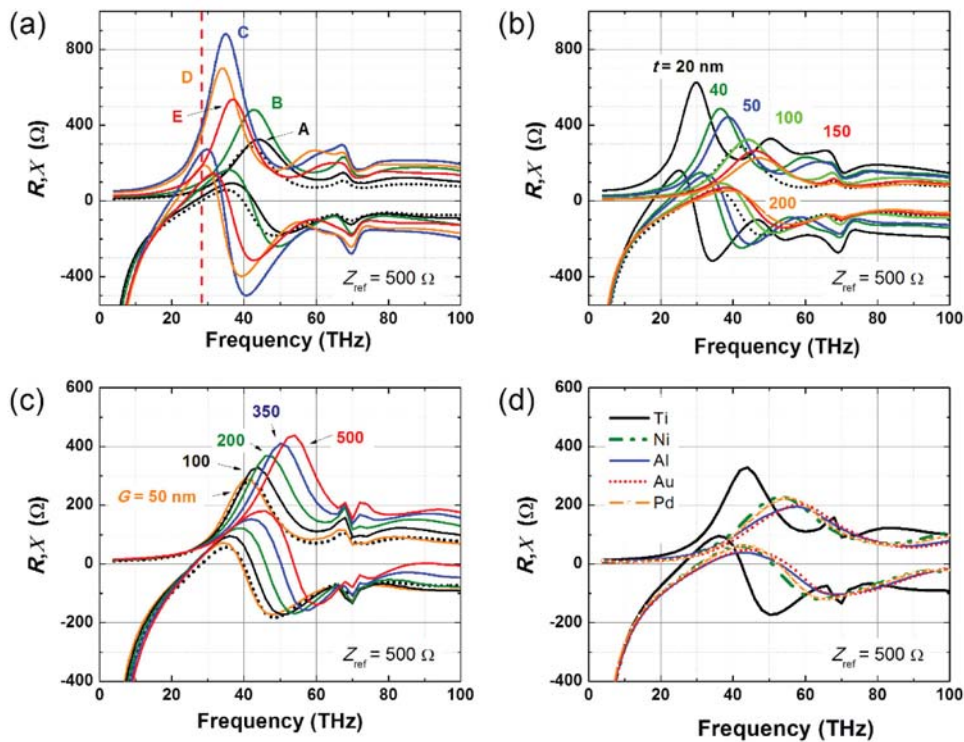

Fig. 3. Frequency dependence of the characteristic impedance for a 3-steps tapered dipole antenna. The real R and imaginary X parts of the impedance are presented as a function of: (a) the geometry structure, (b) the thickness, (c) the gap size, and (d) the type of metal considered for the dipole.

Further, due to their design, all the tapered geometries have a gap that indeed acts as capacitor. The gap capacitance C_{GAP} can be described by a parallel plate capacitor $C_{GAP} = \varepsilon_g A / G$ [38], where G and A are the size and the cross areas of the gap, respectively. The capacitor C_{GAP} is in parallel with the capacitance of the dipoles C_{ANT}, so the gap capacitance tunes the resonant modes of the antennas. Low gap capacitances cause low total capacitances, $C_T = C_{GAP} + C_{ANT}$. If we consider the dipole as an *RCL* circuit, this condition, in turn, shifts the resonant modes towards higher frequencies [39,40]. To underline this behavior, we have tuned the gap capacitance of the geometry A by changing the size of the

gap G. The results presented in Fig. 3(c) show that increasing the gap size leads to resonant modes of higher frequencies as expected.

It is worth noting that the position and amplitude of the resonant modes depend on the considered metal. To highlight this dependence, we evaluate the impedance of the geometry of the type A, in a variety of metals, such as titanium (Ti), nickel (Ni), gold (Au), aluminum (Al) and palladium (Pd). The results, shown in Fig. 3(d), unveil that Ti dipoles exhibit the higher impedances. The influence of the metal can be understood in terms of the conductivity and skin depth of metals [41]. On the one hand, the skin depth determines how localized the resonant current is: a larger skin depth results in a shift of the modes towards lower frequencies [41]. This is, for instance, the case of aluminum dipoles, which exhibit the larger skin depth. On the other hand, the amplitude of the impedance depends on the conductivity of the metal: the lower the DC conductivity of the metal the higher the impedance. In order to approach the use of dipoles for the detection of infrared wavelengths, Ti appears as a natural metal choice due to its high resistance, which can be used to accomplish a better match to high resistive micro-bolometers.

6. Particle swarm optimization of the LWIR tapered dipole

Once we have studied the resonance properties with emphasis on geometry, we exploit and tune the geometrical parameters in order to find the dimensions of the dipoles that match the best the 500 Ω port. In order to perform this optimization process, we use a particle swarm optimization (PSO) program that communicates with the COMSOL Multiphysics numerical solver through an external link. The solver obtains both, the return losses S_{11} and the input impedance Z_{in} of the given geometry, and measures their relevance through a so-called *fitness function f* (see Eq. (1). The PSO optimizer analyzes the fitness function and subsequently updates the nanoantennas dimensions in order to minimize such a function at wavelengths around 10.6 μm. It should be mentioned that the fitness function is here defined in such a manner that its minimum values imply a better impedance match and therefore a better detector performance.

The fitness function *f* suggested here is a quite simple linear combination of the wavelength at the minimal return loss $\lambda_{min(S11)}$ and the reactance X of the dipoles. The expression is given by:

$$f = c_1 \bullet \left| \lambda_{min(S_{11})} - 10.6 \mu m \right| + c_2 \bullet \left| X \right| \qquad (1)$$

where c_1 and c_2 are positive weighting constants that equalize the contribution of the X and the term ($\lambda_{min(S11)}$ - 10.6μm). On the one hand, the first term tunes the return loss minima to the desired wavelength (10.6 μm). On the other hand, due to its absolute value, the second term should vanish when the function is minimized; this term consequently ensures that the nanoantennas are at resonance.

Additionally, some constraints were imposed on the values of the geometrical parameters: (a) $W_1 > W_2 > W_3$, with the aim to confine the electric field and to increase the impedance at the gap, and (b) W_i - W_{i+1} and t >10 nm, in order to introduce some design manufacture feasibility, and (c) $L = 2.2$ μm, to keep constant the length of devices.

In the pursuit of the device improvement, the PSO routine was ran by using as initial conditions the dimensions of the aforementioned A-type geometry. The initial geometry has a fitness function in $f = 52$, and after 300 iterations, f is decreased 17 times to obtain a final value of $f = 13$, as can be seen in Fig. 4(a). In only a few rapid improvements, the algorithm was able to find a geometry whose dimensions can be considered as optimized, showing this manner the effectiveness of the PSO algorithm. The schema of the optimized geometry, whose dimension are $L_1 = 273$ nm, $L_2 = 563$ nm, $L_3 = 162$ nm, $W_1 = 292$ nm, $W_2 = 103$ nm, $W_3 = 97$ nm, $T = 42$ nm and $G = 103$ nm, is shown in Fig. 4(b). The values of the return losses

S_{11} and the real part R of the impedance are shown for some points, particularly, at the pronounced steps of the graph.
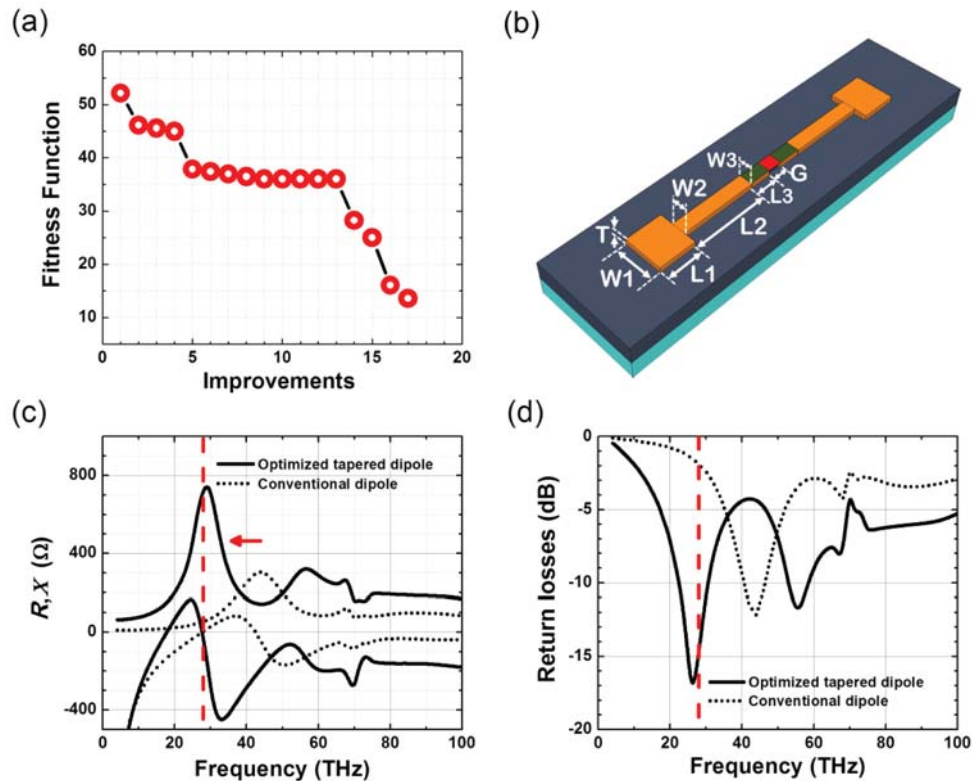

Fig. 4. Optimized Nano-antenna. (a) Evolution of the *fitness function* with the number of *improvements*. (b) Schema of the optimized geometry obtained with the PSO algorithm. (c) Real R and imaginary X parts of the input impedance for the optimized geometry. (d) Return losses.

The match improvement, obtained via the proposed fitness function, can be appreciated by plotting the frequency dependence of both the impedance and return loss for the optimized geometry, and comparing it to the conventional dipole, as seen in Fig. 4(c) and Fig. 4(d). First, from results shown in Fig. 4(c) it can be noted that the odd and even modes (of the optimized geometry) are shifted towards lower frequencies. In particular, the even mode is presented at a frequency ~28.3 THz (10.6 μm), frequency where the detector is desired to operate. Second, the amplitude of the impedance (of the optimized geometry) at the even mode is also increased, and appears to better match that of the port of excitation. Due to this, the losses of power by reflection have been reduced at the wavelength of operation, as shown by the return losses in Fig. 4(d), which have changed from −2 decibels to −15 decibels (i.e. 650%).

On the one hand, the numerical results show that the PSO algorithm does constitute an accurate tool to quickly find geometries that better match the resistance of the port. In a few improvements, the optimization task is accomplished, as stated above. The accuracy of this method entirely relays on how well the fitness function is defined, as we will discuss at the end of this section. On the other hand, the tapered dipole stands out as a good candidate to couple high resistive elements without changing the physical lengths of the devices.

At visible wavelengths, similar methods on similar devices were employed, by El-Toukhy et *al.* [22], in order to optimize the harvesting efficiency of silver nanoantennas, and to improve the coupling between antennas and metal-insulator-metal rectifying diodes of 500 Ω

(at λ = 600 nm). In the impedance analysis, the authors evaluate the resistance R and reactance X as a function of the wavelength (from 400 nm to 600 nm) of a series of tapered dipoles, optimized to match ports with resistance of 500 Ω, 1 kΩ and 2 kΩ, respectively. On the one hand, those results show in a clear manner the multi-resonance behavior of those structures, which holds four resonance modes (2 odd and 2 even modes); in some cases (case for 1 kΩ), those four resonances modes degenerate into three modes. On the other hand, those results permit to underline how much the magnitude of the impedance changes with the geometrical parameters in the visible regime; the magnitude of the impedance can increase to values higher than 2 kΩ by applying slight variations of the geometrical parameters. Despite the similarity between the devices and methods, the results on the LIWR regime are quite different from the visible counterpart. On the one hand, the impedance of the LWIR tapered dipoles behaves more like the impedance of conventional infrared dipoles, the different resonance modes do not degenerate. The two steps of the tapered dipole just adjust the effective length of the structures, without changing the physical length, and tune the magnitude of the impedance. On the other hand, the amplitude of the impedance only changes with notorious changes of the geometrical parameters. This is mainly due to the high refractive index of metals in the LWIR regime. Drastic or important changes of Z_{in} with their geometrical parameters can only be obtained by choosing materials with low refractive index; for instance, the refractive index of titanium at visible wavelengths is $n* = 2.6 + j\ 3.58$ (λ = 600nm), a value that strongly differs from the LIWR counterpart $n* = 4.1 + 20.3j$ (λ = 10.6 μm).

Some remarks concerning the PSO algorithm should be stated. It must be noted that the optimized geometry matches the micro-bolometer in a good degree, but not completely. This is due to the suggested fitness function f, which is a linear combination of the two terms that the PSO algorithm should simultaneously optimize. In this type of optimization processes, the algorithm does not find a solution that satisfies both terms, but rather the weight of their relative importance must be stablished or stated. These types of effects, in which the impedance is not completely coupled, are also observed in other contributions [22].

Finally, to underline the accuracy and usefulness of this method, we compare it to classical standard matching techniques based on transmission lines (TL's), as we will see below.

7. Transmission lines matching

Some coupling techniques used in the radio frequency (RF) regime have been successfully extrapolated to the infrared regime to better match high resistive loads to different types of nanometer antennas. These techniques are based in the use of microstrip transmission lines (TL) inserted between the antenna and the load as impedance matchers [42]. These types of matchers use the fact that the input impedance Z_{in} of the transmission lines varies with length as:

$$Z_{in}(l) = Z_0 \frac{Z_L + Z_0 \tan h(\gamma l)}{Z_0 + Z_L \tan h(\gamma l)} \qquad (2)$$

where Z_0 is the so-called characteristic impedance of the transmission line, Z_L the impedance of the load, and $\gamma = \alpha + j\beta$ is defined by the attenuation α and propagation β constants [43]. By choosing an appropriate length, the input impedance of the transmission line, which is terminated by the load, equals the impedance of the antenna.

With the aim to compare the effectiveness of the TL-based matching technique and the tapered dipole approach, the response of a conventional Ti dipole was studied for different lengths of a transmission line (200, 500, 900, 1400, 2000 and 3200 nanometers), inserted between the dipole and the 500 Ω port as shown in Fig. 5(a).
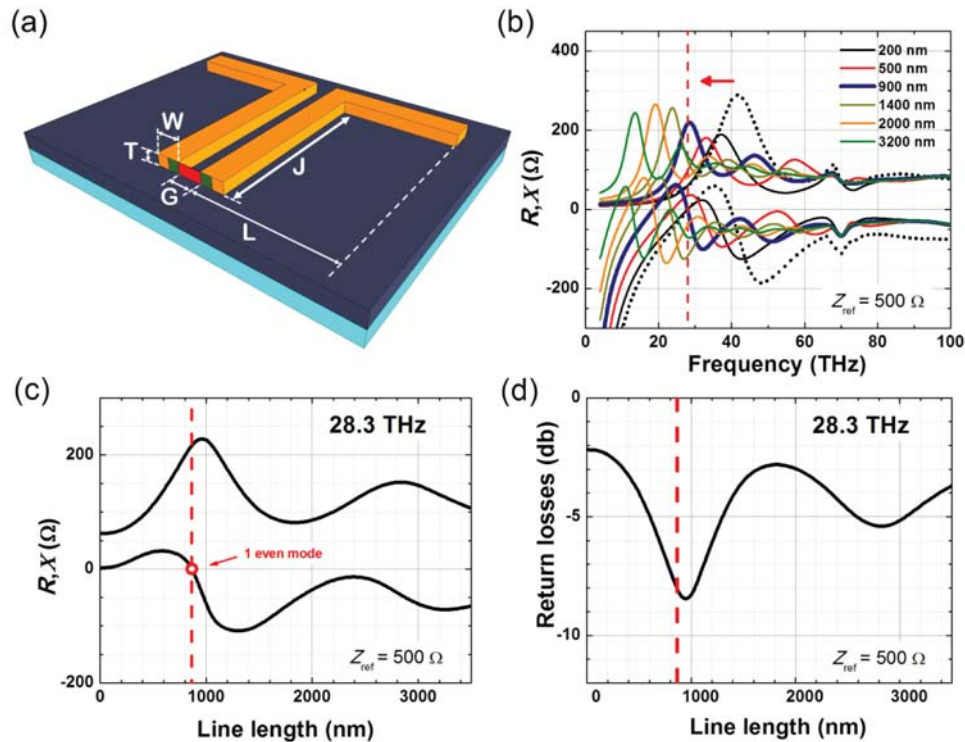
Fig. 5. (a) Schema of a section of transmission line inserted between a conventional half-wave dipole and the 500-Ω lumped port, used as impedance matcher, (b) input impedance of the dipole-coupled transmission line, real R and imaginary parts X, as a function of the frequency (for several line lengths), unveiling the shift of the odd resonance mode towards lower frequencies, (c) input impedance of the dipole-coupled transmission line at 28.3 THz (10.6 μm), real R and imaginary X parts, as function of the line length, revealing the line length that matches better both elements (900nm), and (d) return losses exhibit the device when a 900 nm line is used as impedance matcher.

The impedances that the different sections of the TL exhibit at the port terminals, when they are coupled to the dipole, are numerically evaluated and shown in Fig. 5(b), as a function of the frequency. The numerical results show that the impedance shifts towards lower frequencies as the length of the TL increases. As consequence, the odd and even resonance modes of the dipole-coupled TL shift likewise.

Once the impedance of the different transmission lines was evaluated, the optimal line length that better matches the 500 Ω port can be easily found for the wavelength (or frequency) of interest. For this purpose, both, the impedance and the return losses of the lines are plotted as a function of length in Fig. 5(c) and Fig. 5(d), for a frequency ~28 THz (~10.6 μm). On the one hand, the numerical results in Fig. 5(d), show that the losses by reflection are minimal when a 900 nm long TL is used; length at which the reactance vanishes. On the other hand, the results in Fig. 5(c), unveil that the return losses are minimal for the even resonance mode of the dipole-coupled transmission line. It must be noted that this optimization technique does not completely match the impedance of the port and the dipole since the resistance of the even mode is around 230 Ω, which is about half the value of the resistance port. The best performance that an optimized detector could exhibit implies return losses around −8 dB.

It is worth noting that use of transmission lines as matchers leads to infrared detectors that operate on the even resonance. The same task is achieved, as has been showed above, by using tapered dipoles with the appropriate design. Both techniques are based on the

impedance properties that exhibit the devices at the even mode. However, by comparing the performance of the devices optimized with the PSO algorithm (−15 dB) and those optimized by using the TL's (−8 dB), it can be concluded that the tapered design exhibit much better results. Moreover, due to their design, the experimental realization implies the use of much less resources than the transmission lines. Tapered dipoles therefore open the route towards an efficient match at infrared and visible wavelengths.

8. Conclusions

A three-stepped dipole nano-antenna, coupled to a nano-bolometer element, was investigated as a sensing device designed to operate in the long-wavelength infrared band. The multi-resonant response of the device was tuned, via its geometrical parameters, in order to meet specific impedance requirements at the antennas terminals, resulting in an improved impedance matching to the high-resistive micro-bolometer. The resonant modes, impedance and return loss were firstly evaluated on conventional half-dipoles coupled to resistive elements; the results showed that, at high resistance, energy transfer is optimal for even resonant modes and that power loss is high for odd modes. Since the presence of high resistive elements shifts the resonant modes to values where the performance quenches, a tapered dipole antenna design was introduced as a strategy to tune the impedance of the antennas. Numerical simulations of the tapered antennas demonstrate that the steps introduced in the conventional dipole results in both, the shift of the resonant modes towards lower frequencies and an increase of the impedance. A so-called particle swarm optimization (PSO) algorithm was subsequently introduced to optimize the geometrical parameters of the antenna in order to obtain the best match to a 500 Ω port, which emulates the bolometer resistance. The optimized geometry results in the even resonance mode shifted towards the desired operation frequency (28THz) and in a reduction of 650% in the return loss. The proposed architecture is then compared to the approach that uses transmission lines (TL) as matchers, whose analysis was also numerically conducted here; the 3-step tapered antenna dipole being up to 200% more effective than the TL and its feasibility less demanding. Tapered dipoles therefore open the route towards an efficient match at infrared and visible wavelengths.

Acknowledgments

Disclosures

The authors declare that there are no conflicts of interest related to this article.

References

1. A. Rogalski, P. Martyniuk, and M. Kopytko, "Challenges of small-pixel infrared detectors: a review," Rep. Prog. Phys. **79**(4), 046501 (2016).
2. J. A. Ratches, "Current and Future Trends in Military Night Vision Applications," Ferroelectrics **342**(1), 183–192 (2006).
3. T. M. Walcott, *Bolometers: Theory, Types, and Applications* (Nova Sci., 2011).
4. G. D. Skidmore, C. J. Han, and C. Li, "Uncooled microbolometers at DRS and elsewhere through 2013," Proc. SPIE **9100**, 910003 (2014).
5. H. Takeya, J. Frame, T. Tanaka, Y. Urade, X. Fang, and W. Kubo, "Bolometric photodetection using plasmon-assisted resistivity change in vanadium dioxide," Sci. Rep. **8**(1), 12764 (2018).
6. A. Subrahmanyam, Y. Bharat Kumar Reddy, and C. L. Nagendra, "Nano-vanadium oxide thin films in mixed phase for microbolometer applications," J. Phys. D Appl. Phys. **41**(19), 195108 (2008).
7. A. J. Syllaios, T. R. Schimert, R. W. Gooch, W. L. McCardel, B. A. Ritchey, and J. H. Tregilgas, "Amorphous Silicon Microbolometer Technology," Mat. Res. Soc. Symp. Proc. **609**, A14.4 (2000).
8. U. Sassi, R. Parret, S. Nanot, M. Bruna, S. Borini, D. De Fazio, Z. Zhao, E. Lidorikis, F. H. L. Koppens, A. C. Ferrari, and A. Colli, "Graphene-based mid-infrared room-temperature pyroelectric bolometers with ultrahigh temperature coefficient of resistance," Nat. Commun. **8**, 14311 (2017).

9.   Q. Han, T. Gao, R. Zhang, Y. Chen, J. Chen, G. Liu, Y. Zhang, Z. Liu, X. Wu, and D. Yu, "Highly sensitive hot electron bolometer based on disordered graphene," Sci. Rep. **3**(1), 3533 (2013).
10. M. Mahjouri-Samani, Y. S. Zhou, X. N. He, W. Xiong, P. Hilger, and Y. F. Lu, "Plasmonic-enhanced carbon nanotube infrared bolometers," Nanotechnology **24**(3), 035502 (2013).
11. A. Kawakami, H. Shimakage, J. Horikawa, M. Hyodo, S. Saito, S. Tanaka, and Y. Uzawa, "Fast response of superconducting hot-electron bolometers with a twin-slot nano-antenna for mid-infrared operation," AIP Adv. **6**(12), 125120 (2016).
12. V. Yu. Zerov, V. G. Malyarov, and I. A. Khrebtov, "Antenna-coupled microbolometers," J. Opt. Technol. **78**(5), 308–316 (2011).
13. I. Codreanu and G. D. Boreman, "Integration of microbolometers with infrared microstrip antennas," Infrared Phys. Technol. **43**(6), 335–344 (2002).
14. P. Renoux, S. A. Jónsson, L. J. Klein, H. F. Hamann, and S. Ingvarsson, "Sub-wavelength bolometers: Uncooled platinum wires as infrared sensors," Opt. Express **19**(9), 8721–8727 (2011).
15. J. Wei, D. Olaya, B. S. Karasik, S. V. Pereverzev, A. V. Sergeev, and M. E. Gershenson, "Ultrasensitive hot-electron nanobolometers for terahertz astrophysics," Nat. Nanotechnol. **3**(8), 496–500 (2008).
16. F. J. Gonzalez, C. S. Ashley, P. G. Clem, and G. D. Boreman, "Antenna-coupled microbolometer arrays with aerogel thermal isolation," Infrared Phys. Technol. **45**(1), 47–51 (2004).
17. F. B. P. Niesler, J. K. Gansel, S. Fischbach, and M. Wegener, "Metamaterial metal-based bolometers," Appl. Phys. Lett. **100**(20), 203508 (2012).
18. C. F. Middleton and G. D. Boreman, "Technique for thermal isolation of antenna-coupled infrared microbolometers," J. Vac. Sci. Technol. B **24**(5), 2356–2359 (2006).
19. F. J. González, B. Ilic, and G. D. Boreman, "Antenna-coupled microbolometers on a silicon-nitride membrane," Microw. Opt. Technol. Lett. **47**(6), 546–548 (2005).
20. J. P. Rice, E. N. Grossman, and D. A. Rudman, "Antenna-coupled high-Tc air-bridge microbolometer on silicon," Appl. Phys. Lett. **65**(6), 773–775 (1994).
21. F. J. González, M. Abdel-Rahman, and G. D. Boreman, "Antenna-coupled VOx thin-film microbolometer array," Microw. Opt. Technol. Lett. **38**(3), 235–237 (2003).
22. Y. M. El-Toukhy, M. Hussein, M. F. O. Hameed, A. M. Heikal, M. M. Abd-Elrazzak, and S. S. A. Obayya, "Optimized tapered dipole nanoantenna as efficient energy harvester," Opt. Express **24**(14), A1107–A1122 (2016).
23. Y. M. El-Toukhy, M. Hussein, M. F. O. Hameed, and S. S. A. Obayya, "Characterization of Asymmetric Tapered Dipole Nanoantenna for Energy Harvesting Applications," Plasmonics **13**(2), 503–510 (2018).
24. M. Gustafsson and C. Sohl, "Summation rules for the antenna input impedance," in Proceedings of IEEE Antennas and Propagation Society International Symposium (IEEE, 2008), pp. 1–4.
25. E. D. Palik, *Handbook Of Optical Constants of Solids* (Academic Press, 1985).
26. R. Eberhart and J. Kennedy, "A new optimizer using particle swarm theory," in Proceedings of IEEE International Symposium on Micro Machine and Human Science (IEEE, 1995), pp. 39–43.
27. C. Forestiere, M. Donelli, G. F. Walsh, E. Zeni, G. Miano, and L. Dal Negro, "Particle-swarm optimization of broadband nanoplasmonic arrays," Opt. Lett. **35**(2), 133–135 (2010).
28. R. Ruiz-Cruz, E. N. Sanchez, F. Ornelas-Tellez, A. G. Loukianov, and R. G. Harley, "Particle Swarm Optimization for Discrete-Time Inverse Optimal Control of a Doubly Fed Induction Generator," IEEE Trans. Cybern. **43**(6), 1698–1709 (2013).
29. R. Méjard, A. Verdy, O. Demichel, M. Petit, L. Markey, F. Herbst, R. Chassagnon, G. Colas-des-Francs, B. Cluzel, and A. Bouhelier, "Advanced engineering of single-crystal gold nanoantennas," Opt. Mater. Express **7**(4), 1157–1168 (2017).
30. S. Bagheri, K. Weber, T. Gissibl, T. Weiss, F. Neubrech, and H. Giessen, "Fabrication of Square-Centimeter Plasmonic Nanoantenna Arrays by Femtosecond Direct Laser Writing Lithography: Effects of Collective Excitations on SEIRA Enhancement," ACS Photonics **2**(6), 779–786 (2015).
31. S. Aksu, A. A. Yanik, R. Adato, A. Artar, M. Huang, and H. Altug, "High-Throughput Nanofabrication of Infrared Plasmonic Nanoantenna Arrays for Vibrational Nanospectroscopy," Nano Lett. **10**(7), 2511–2518 (2010).
32. F. J. González, J. Alda, J. Simón, J. Ginn, and G. Boreman, "The effect of metal dispersion on the resonance of antennas at infrared frequencies," Infrared Phys. Technol. **52**(1), 48–51 (2009).
33. L. Novotny, "Effective Wavelength Scaling for Optical Antennas," Phys. Rev. Lett. **98**(26), 266802 (2007).
34. C. A. Balanis, *Antenna Theory* (Wiley Interscience, 2005).
35. J. A. Bean, A. Weeks, and G. D. Boreman, "Performance Optimization of Antenna-Coupled Al/AlOx/Pt Tunnel Diode Infrared Detectors," IEEE J. Quantum Electron. **47**(1), 126–135 (2011).
36. J. A. Bean, B. Tiwari, G. H. Bernstein, P. Fay, and W. Porod, "Thermal infrared detection using dipole antenna-coupled metal-oxide-metal diodes," J. Vac. Sci. Technol. B **27**(1), 11–14 (2009).
37. P. K. Ghosh, D. T. Debu, D. A. French, and J. B. Herzog, "Calculated thickness dependent plasmonic properties of gold nanobars in the visible to near-infrared light regime," PLoS One **12**(5), e0177463 (2017).
38. M. S. Eggleston, K. Messer, L. Zhang, E. Yablonovitch, and M. C. Wu, "Optical antenna enhanced spontaneous emission," Proc. Natl. Acad. Sci. U.S.A. **112**(6), 1704–1709 (2015).
39. D. P. Fromm, A. Sundaramurthy, P. James Schuck, G. Kino, and W. E. Moerner, "Gap-Dependent Optical Coupling of Single Bowtie Nanoantennas Resonant in the Visible," Nano Lett. **4**(5), 957–961 (2004).

40. O. Scholder, K. Jefimovs, I. Shorubalko, C. Hafner, U. Sennhauser, and G.-L. Bona, "Helium focused ion beam fabricated plasmonic antennas with sub-5 nm gaps," Nanotechnology **24**(39), 395301 (2013).
41. H. Guo, T. P. Meyrath, T. Zentgraf, N. Liu, L. Fu, H. Schweizer, and H. Giessen, "Optical resonances of bowtie slot antennas and their geometry and material dependence," Opt. Express **16**(11), 7756–7766 (2008).
42. P. M. Krenz, B. Tiwari, G. P. Szakmany, A. O. Orlov, F. J. González, G. D. Boreman, and W. Porod, "Response Increase of IR Antenna-Coupled Thermocouple Using Impedance Matching," IEEE J. Quantum Electron. **48**(5), 659–664 (2012).
43. H. J. Visser, *Antenna Theory and Applications* (John Wiley & Sons, 2012).